Check for updates

OPEN

# Robust half-metallicity and magnetic phase transition in Sr_2CrReO_6 via strain engineering

Qurat-Ul Ain, Shahnila Naseem & Safdar Nazir✉

Using ab-initio calculations, the electronic and magnetic properties of double perovskite oxide Sr_2CrReO_6 with two type of strains: biaxial (along the [110]-direction) and hydrostatic (along [111]-direction) are investigated. The ground state of the unstrained system is half-metallic ferrimagnetic, due to a strong antiferromagnetic (AFM) coupling between Cr and Re atoms within both (GGA and GGA+U) exchange-correlation potentials. It is demonstrated that the robustness of half-metallicity can be preserved under the influence of both biaxial and hydrostatic strains. Interestingly, a transition from ferri-to-ferromagnetic is established due to Re spin flipping to that of the Cr ion (i.e. Cr and Re spin becomes parallel) within the GGA+U method for both biaxial and hydrostatic tensile strains of $\geq +2\%$. The strong confinement of orbitals due to tensile strain results in the decrease of electron hopping which further reduced the AFM coupling strength between Cr and Re atoms, this leads to a ferri-to-ferromagnetic transition. However, the GGA scheme holds the ferrimagnetic state with both kinds of strains. This work shows that tensile strain is a feasible way to optimize the magnetic properties of perovskite oxides, which are presumed to be beneficial for spintronic technology.

Half-metallic (HM) ferromagnetic (FM) materials (where one spin channel shows a metallic behavior and another one contains an insulating or semiconducting nature, refers to 100% spin polarized)[1–3] have been attracted a great interest due to their functional technological applications in spintronics such as colossal magnetoresistance[4,5] and spin-transfer torque magnetic random access memory[6–8]. As recently Kumari et al.[9] experimentally observed that perovskite manganite family such as $La_{0.7}Sr_{0.3}MnO_3$ demonstrated the bipolar resistive switching behavior. Similarly, a recent review on two-dimensional spinterfaces and magnetic-interfaces exhibits a wide range of applications in spintronics such magnetic tunnel junctions[10]. In this respect, double perovskites $A_2BB'O_6$ (A = alkaline earth or rare earth metal atoms and $BB' = 3/(4, 5, 6)d$ transition metals such as B = Fe, Cr, Mn, Co, and Ni; $B' = $ Mo, Re, Os, and W) have been considered hot candidates because they show a HM ferrimagnetic (FiM) ground state having a relatively high Curie temperature (T_c) of 300–420 K[11–16]. In 1963, the discovery of metallic FiM with a reasonable T_c of 410-450 K in Sr_2FeMoO_6 (SFMO)[17,18], substantially stimulated the researcher to synthesize or predict new double perovskites with novel magnetic properties.

Among the double perovskite oxides, Cr-based FiM $A_2CrB'O_6$ (A = Sr and Ca; $B' = $ Mo, W, and Re) exhibits potential applications in spintronic devices such as low-field magnetoresistive sensors or magnetic tunnel junctions[19]. Usually, Cr^{+5} ($3d^5$ having S = 5/2) shows strong antiferromagnetic (AFM) coupling with Mo^{+5} ($4d^5$ having S = 1/2), W^{+5} ($5d^5$ having S = 1/2), and Re^{+5} ($5d^5$ having S = 1/2) atoms, which results in FiM state. In this line, HM FiM or FM state having a total magnetic moment of 0.86(0.89) μ_B/f.u with a highest T_C of 635 K is observed in Sr_2CrReO_6 (SCRO)[12,20–22] in contrast to very closely related Ca_2CrReO_6, which shows insulating behavior in both experiments[12,20] and theoretical work[23]. It is observed that SCRO contains very high T_C as compared to other closely related Sr_2CrWO_6 having a T_C of 400 K[24,25]. However, Krockenberger et al.[26,27] observed the highest T_C of 725 K with high spin-polarization in Sr_2CrOsO_6 and it is established that HM behavior in FiM double perovskite can be changed to insulating behavior. In contrast, the first-principles calculations exhibit the semi-metallic AFM state in the Sr_2CrTO_6 (T = Os and Ru) system due to a strong spin-orbit coupling[28]. Moreover, a HM and metallic FiM (AFM coupling is favorable between Cr and Re atoms) states are predicted using density functional theory (DFT) calculations in SCRO with magnetic moments of 1.0 and 1.28 μ_B with and without spin-orbit coupling, respectively[29]. Later on, Majewski et al. experimentally confirmed the FiM state in SCRO at a low temperature of 10 K[22].

Department of Physics, University of Sargodha, Sargodha 40100, Pakistan. ✉email: safdar.nazir@uos.edu.pk

1
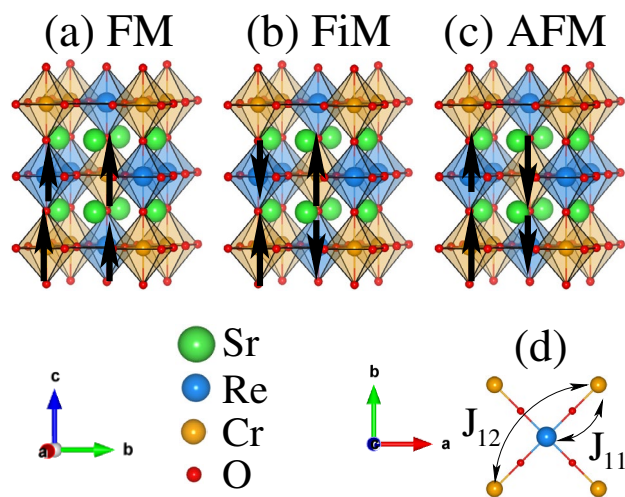
Figure 1. Schematic representation of the double perovskite structures of Sr_2CrReO_6 in (**a**) ferromagnetic (FM), (**b**) ferrimagnetic (FiM), and (**c**) antiferromagnetic (AFM) ordering. The octahedral surroundings of the Cr and Re atoms are visualized in orange and blue colored polyhedron, respectively. (**d**) the top view in the ab-plane demonstrating the spin-coupling between Cr-Re (J_{11}) via oxygen and indirect Cr-Cr (J_{12}) atoms. The x, y, and z-axes are along the crystallographic a, b, and c-directions, respectively. The x and z-axis (a and c-directions) are pointing towards the observer in (**a, b**) and (**c**), respectively.

It is experimentally[30–37] and theoretically[38–45] found that strain often has a substantial influence on the electronic and magnetic properties of the systems, when an epitaxially films like $LaAlO_3$, SFMO, and $SrMoO_4$ grown on the $SrTiO_3$(MgO) substrate. As, Borges et al.[30] experimentally observed that the magnetic moment in SFMO thin film reduces from its integral value due to strain exerted by substrates on film, which leads a transition from HM FM to FM metallic (FMM) state. Fix et al.[31] experimentally and theoretically determined that HM state in SFMO thin film vanish, when it is grown on the $SrTiO_3$ (001) substrate. Moreover, the variation in the structural properties of SFMO thin film with biaxial strain is observed, when it is grown on different substrates such as MgO, $LaAlO_3$, and $SrTiO_3$[32]. It is theoretically found that a hydrostatic pressure upto 33-36 GPa on the SFMO, leads the Fe spin state from high to low and results in a transition from HM FiM to non-magnetic semiconductor state[39]. However, the system becomes metallic above 45 GPa. Similarly, Lu et al. theoretically predicted a magnetic phase transition in SFMO from FiM to FM for a tensile of $\geq +8\%$, where Mo spin transform from intermediate-to-low spin state[41]. A recent experiment exhibits that SCRO film is showing the semiconducting behavior with energy gap (E_g) of 0.21 eV at a very low temperature of 2 K, when grown on the STO (lattice mismatch was only 0.05% between the film and the substrate)[46]. This is in contrast to the previous experiments[12,20,21,47,48], which show HM FiM state. Along with this, a high pressure phase of SCRO has been studied both experimentally and theoretically by Olsen et al.[49]. It is found that system shows pseudocubic structure at low pressure, while the tetragonal phase becomes stable at high pressure. Hence, electronic and magnetic behvaior in these compounds is still under debate. Thus, the above mentioned experimental and theoretical facts motivated us to focus on the lesser-explored strained modulated physical properties of SCRO.

In this work, we studied the impact of two types of strains: biaxial and hydrostatic on the electronic and magnetic properties of SCRO employing first-principles DFT calculations. We proposed that by applying a biaxial tensile strain of $\geq +2\%$, a magnetic transition from HM FiM to HMF state occurs due to Re spin transition from intermediate spin-state to low-spin state. On the other hand, a HM FiM to FMM transition is established for a hydrostatic tensile strain of $+2\%$, while for $\geq +3\%$ system becomes HMF. This kind of spin flipping has many novel applications in data storage devices, switches, and optical displays[50].

Results and discussion

Structural details. Bulk SCRO crystallizes in a tetragonal symmetry having space group No. 139 (I4/mmm) with experimental lattice constants of $a = 5.52$ and $c = 7.82$ Å[20]. The Sr, Cr, Re, O1, and O2 occupied $4d(1/2, 0, 1/4)$, $2a(0, 0, 0)$, $2b(0, 0, 1/2)$, $8h(0.249, 0.249, 1/2)$, and $4e(0, 0, 0.254)$ atomic positions, respectively. The schematic representation of SCRO crystal structures in FM, FiM, and AFM spin ordering are shown in Fig. 1a–c, respectively. For the case of FM structure, the spins of Cr and Re ions are align in-plane and out-of-plane directions and support with each other (see Fig. 1a). In FiM spin ordering, Cr and Re atoms are anti-align (see the arrowhead) within both in-plane and out-of-plane directions. However, Cr atoms are ferromagnetically (i.e. parallel to each other) coupled with each other at the diagonal. Similarly, Re atoms also have the same spin magnetization at the diagonal site, see Fig. 1b. In AFM spin ordering, Cr and Re atoms are anti-align and align for in-plane and out-of-plane directions, respectively. However, the diagonal atoms are showing the AFM coupling with each other, see Fig. 1c. It is very important to note that in both (FiM and AFM) magnetic ordering, the spin magnitude of Cr is larger than that of Re (compare the magnitude of the arrows in both cases). Along
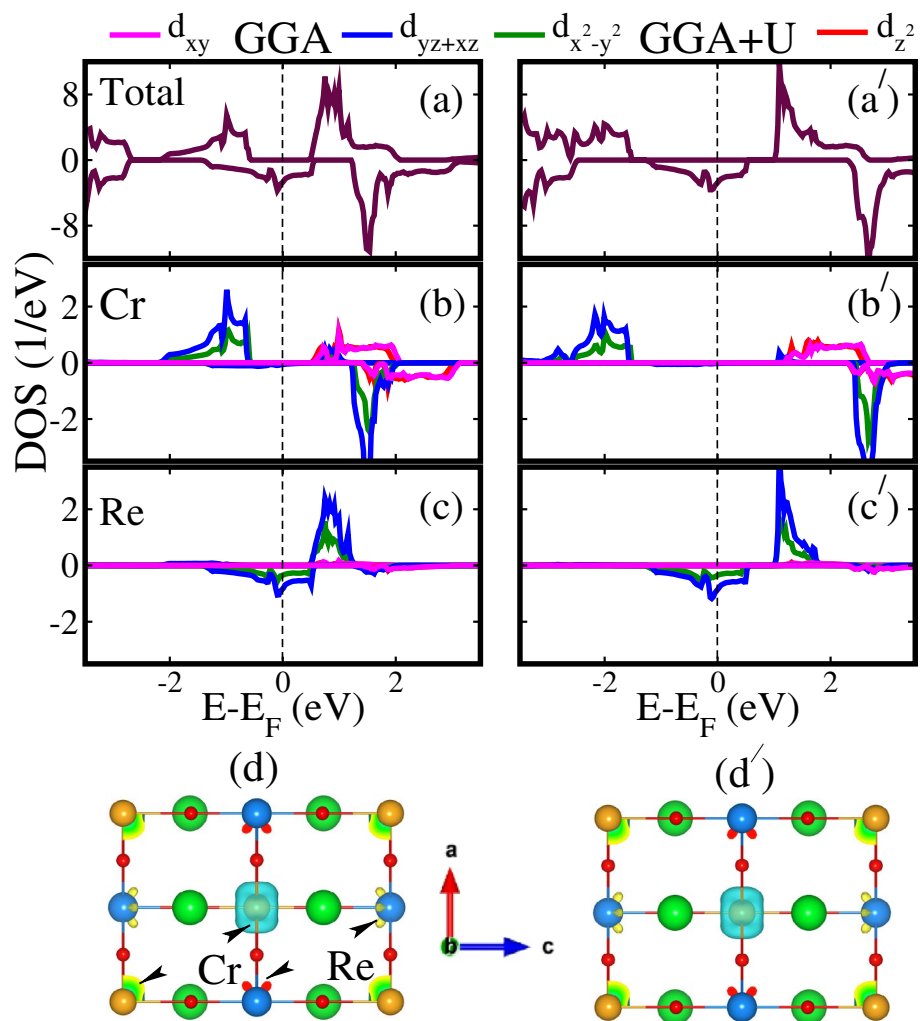
Figure 2. Calculated GGA/GGA+U spin-polarized (**a, a′**) total and orbital resolved partial (**b, b′**) Cr $3d$ and (**c, c′**) Re $5d$ density of states (DOS) of Sr_2CrReO_6 in a FiM spin oredering. (**d, d′**) represents the spin density difference (difference between spin-majority and spin-minority channels) for the top view in the ac-plane. The same iso-value of $0.05e/Å^3$ is used to produce these spin distribution plots. The Fermi level is shown by the vertical dashed line at 0 eV in each DOS figure. The x, y, and z-axes are along the crystallographic a, b, and c-directions, respectively. The y-axis (b-direction) is pointing towards the observer.

with this, two important couplings J_{11} (between Cr and Re atoms via oxygen) J_{12} (indirect coupling between Cr and Cr atoms) in the ab-plane also display in Fig. 1d.

Unstrained system. First, we determined the energetically stable magnetic ordering in SCRO by comparing the total energies of FM, FiM, and AFM states as $\Delta E_1/\Delta E_2 = E_{FiM} - E_{FM}/E_{FiM} - E_{AFM}$. The computed values of $\Delta E_1/\Delta E_2$ are $-3.60/-3.72$ and $-3.35/-4.41$ meV having corresponding T_{C1} and T_{C2} 27.9/28.8 and 27.1/34.1 K within GGA and GGA+U methods, respectively. The T_C is calculated by using the Eqn. 2 as mention in the recent work of Nair et al.[51]. The "−" sign of ΔE indicates that AFM coupling between diagonal Cr atoms is not favorable and also between Re (i.e. both Cr and Re spins wants to align in the same direction at the diagonal). Moreover, this also shows that Cr and Re spins want to be remain anti-align along the in-plane as well as out-of-plane directions. Therefore, FiM magnetic spin ordering is energetically more stable as compared to FM and AFM structures in both cases. Hence, FiM magnetic structure of SCRO is taken into account for further investigations. The calculated spin-polarized total and orbital resolved partial density of states (TDOS and PDOS) of unstrained (0%) SCRO within stable FiM spin ordering for GGA and GGA+U methods are shown in Fig. 2. From Fig. 2a, a′, one can see that the system exhibits HM behavior within both GGA and GGA+U methods, respectively. Spin minority TDOS are contributing to the metallicity, while majority channel remains insulator in both cases. However, the computed E_g of 2.59 eV in a spin-majority channel with GGA+U is much higher than that of 1.01 eV for GGA. Our calculated TDOS are in good agreement with the previously reported theoretical DFT works[29,52–54] and experimental observations[12,21,22], where the authors confirm the HM nature of the system.

In a perfect octahedral crystal field, the Cr/Re 3/5d states split into triply t_{2g} (d_{xy}, d_{xz}, and d_{yz}) and doubly e_g ($d_{x^2-y^2}$ and $d_{3z^2-r^2}$) degenerate states. However, here CrO$_6$/ReO$_6$ octahedron distorted and O$_h$ symmetry reduced to D$_4h$, which degraded the Cr/Re 3/5d orbitals degeneracy. Therefore, the t_{2g} states further split into singlet d_{xy} and doubly (d_{xz} and d_{yz}) non-degenerate states. Similarly, e_g states split into singlet $d_{x^2-y^2}$ and $d_{3z^2-r^2}$ non-degenerate states. Our results show that Cr 3d orbitals are not contributing to the metallic channel (spin-minority) within both GGA and GGA+U as display in Fig. 2b, b$'$, respectively. On the other hand, Re d_{yz+xz} and $d_{x^2-y^2}$ are mainly responsible for conductivity in the spin-minority channel and also show a strong hybridization around the Fermi level (E_F) for both GGA and GGA+U methods as shown in Fig. 2c, c$'$, respectively. Moreover, Re d_{yz+xz} and $d_{x^2-y^2}$ states become more confine near E_F in the case of GGA+U as compared to GGA, which enhanced the magnitude of the moment. For more deep understanding, we plotted the spin difference densities (the difference between spin-majority and spin-minority channels) plots for the top view in the ac-plane within GGA and GGA+U approaches in Fig. 2d, d$'$, respectively. The more densities around Cr atoms in both cases confirm that main contributions to the total magnetic moment comes from Cr with a small from Re ion, whcich confirms the DOS in Fig. 2b, b$'$, c, c$'$.

The calculated total magnetic moment is 1.0 μ_B/f.u. within both GGA and GGA+U methods, which confirms the HM nature of SCRO and also in a good agreement with experimentally/theoretically found value of 0.9/1.0 μ_B/f.u.[21,48]. The partial moments on the Cr and Re atoms are 2.09/2.44 and $-0.83/-1.06$ μ_B for GGA/GGA+U scheme, respectively. The "$-$" sign in Re moment indicates that its spin is ant-align as well as with smaller in magnitude than that of Cr, which confirms the FiM ordering in SCRO. Our computed Cr(Re) moments are very close to the previously calculated[29,52–54] and experimentally[22,48] observed values.

Next, we investigated the influence of biaxial (along the [110]-direction) and hydrostatic strains (along the [111]-direction) on the electronic and magnetic properties of SCRO. We modeled the biaxial and hydrostatic strains in the range of -5% to $+5\%$ by tunning the lattice parameters in the ab-plane and along the three axis (x, y, z), respectively. The "$-$" and "$+$" signs indicate compressive and tensile strains, respectively.

Strained systems. *Structure stability.* First, we examined the structural stability of the unstrained and strained SCRO systems in a FiM spin ordering by calculating the enthalpies of formation (ΔH_f) as:

$$\Delta H_f = E_t^{Sr_2CrReO_6} - \frac{1}{2}E_t^{Sr} - E_t^{Cr} - E_t^{Re} - \frac{6}{2}E_t^{O_2} \tag{1}$$

where $E_t^{Sr_2CrReO_6}$ is the total energy of SCRO, while E_t^{Sr}, E_t^{Cr}, E_t^{Re}, and $E_t^{O_2}$ are the per-atom energies of the most stable low-temperature phases of Sr, Cr, Re, and O ions, respectively. The calculated ΔH_f of SCRO as a function of biaxial and hydrostatic strains within both (GGA and GGA+U) schemes are plotted in the Supporting Information (SI) of Fig. 1Sa, b, respectively. One can see that the negative values of ΔH_f in all cases confirmed the structure stability of the systems with respect to applied strains and can be easily grow in the experiment. However, biaxial strain systems show more stability because of lower energies as compared to hydrostatic ones (correlate the Fig. 1Sa, b in the SI). Our results also show that structure stability increases when both biaxial and hydrostatic strains are adjusted from -5% to $+5\%$, as ΔH_f becomes more negative. Furthermore, it is also noted that GGA+U method produces lower ΔH_f values than that of GGA in both types of strains (biaxial and hydrostatic), which means that systems exhibit higher solidity in this scheme.

Electronic properties. To qualitatively shows the changes in the electronic properties of SCRO with various biaxial strains, we produced the spin-polarized TDOS for biaxial tensile strains of $+1\%$, $+2\%$, $+3\%$, $+4\%$, and $+5\%$ in Fig. 3a, a$'$, b, b$'$), c, c$'$, d, d$'$, and e, e$'$) within GGA/GGA+U method, respectively. The GGA calculated TDOS for biaxial tensile strains of $+1\%$ to $+5\%$, almost showing the same behavior as found in unstrained one (0%), compare Fig. 3a–e with Fig. 2a. A similar pattern of TDOS computed with GGA for biaxial compressive strains (ranging from -1% to -5%) is also found, see Fig. 2S of SI. This means that GGA keeps the HM nature of SCRO as a function of both (compressive and tensile) biaxial strains (Fig. 2Sa, b and Fig. 3a–e) as determined in unstrained system (Fig. 2a), where the spin-majority channel is insulator and spin-minority is metallic. In the case of GGA+U method, biaxial tensile strain of $+1\%$ produces almost the same TDOS as found in unstrained (0%) system (compare Figs. 3a$'$ and 2a$'$). Surprisingly, the spin-majority channel becomes metallic and spin-minority is showing the insulating behavior with a large E_g of 2.14 eV for a biaxial tensile strain of $+2\%$ to $+5\%$ (see Fig. 3b$'$–e$'$)) in contrast to calculated GGA TDOS for -1% to -5% (Fig. 2Sa–e of the SI) and $+1\%$ to $+5\%$ (Fig. 3a, e) as well as with GGA+U scheme for -1% to -5% (Fig. 2Sa$'$–e$'$ of the SI) and $+1\%$ (Fig. 3a$'$) biaxial strains. Hence, one can conclude that the system maintains its HM nature by adjusting the biaxial strain of -5% to $+5\%$ along the [110]-direction (in the ab-plane) within both methods.

Next, the calculated spin-polarized TDOS for hydrostatic tensile strains of $+1\%$, $+2\%$, $+3\%$, $+4\%$, and $+5\%$ are plotted in Fig. 4a, a$'$, b, b$'$, c, c$'$, d, d$'$, e, e$'$ within GGA/GGA+U method, respectively. Similar to biaxial strain results, the TDOS produced with GGA for the hydrostatic strain of $+1\%$ to $+5\%$ (see Fig. 4a–e), almost showing the identical pattern as found in the unstrained (0%) system (Fig. 2a). Moreover, calculated GGA+U calculated TDOS for the hydrostatic strain of $+1\%$ also exhibits the same trend (compare Figs. 4a$'$ and 2a$'$). Interestingly, a HM to metallic and then metallic to HM transition is established for the hydrostatic tensile strains of $+2\%$ and $+3\%$ to $+5\%$ for GGA+U method as plotted in Fig. 4b$'$ and c$'$ to e$'$, respectively. At $+2\%$ hydrostatic tensile strain, spin-majority channel becomes metallic as found in the case of $+2\%$ biaxial tensile strain for GGA+U (Fig. 3b$'$). However, few spin-minority TDOS are also crossing the E_F from conduction to valence band (see Fig. 4b$'$), which makes the system metallic in contrast to biaxial strain (Fig. 3b$'$). Surprisingly, the spin-minority TDOS shifts toward the higher energies in the conduction band for $+3\%$ hydrostatic tensile strain with E_g of 2.12 eV and system becomes again HM (Fig. 4c$'$) and also for higher strains (i.e. $+4\%$ (Fig. 4d$'$)
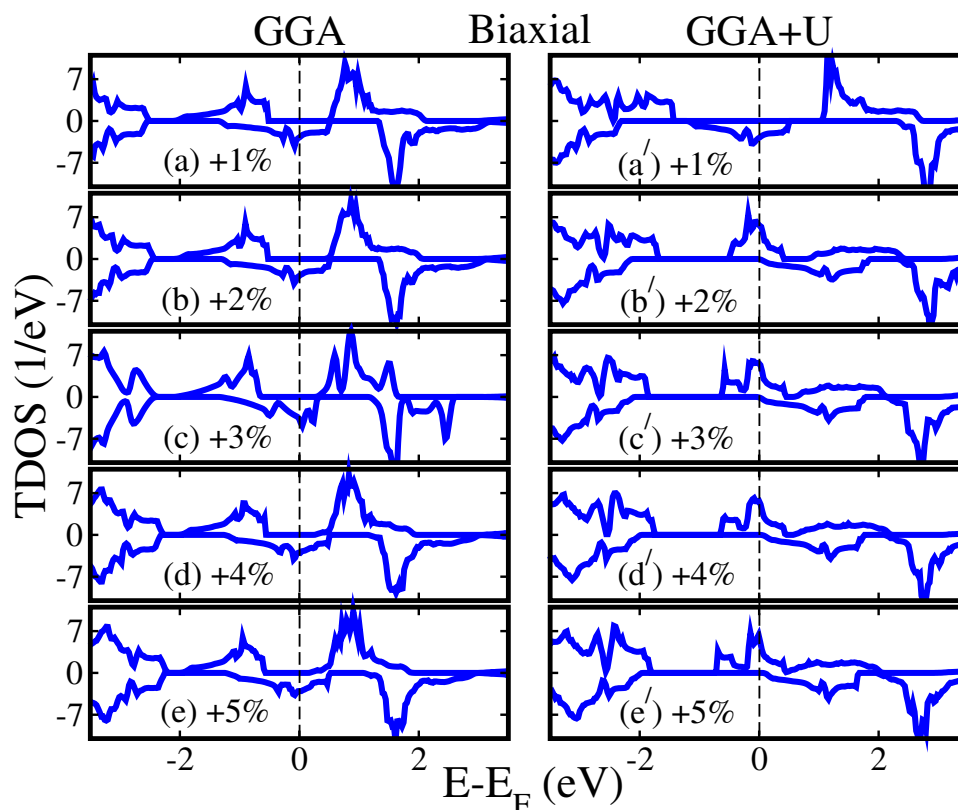
Figure 3. Calculated GGA/GGA+U spin-polarized total density of states (TDOS) of Sr_2CrReO_6 for (**a, a′**) +1%, (**b, b′**) +2%, (**c, c′**) +3%, (**d, d′**) +4%, and (**e, e′**) +5% biaxial tensile strains along [110]-direction (in the ab-plane).

and +5% (Fig. 4e′). Moreover, for hydrostatic compressively strain systems ranging from −1% to −5%, the GGA and GGA+U calculated spin-polarized TDOS are plotted in Fig. 3Sa–e and a′–e′ of the SI, respectively, which almost showing the same behavior as found in the case of biaxially strained systems (Fig. 2S of the SI).

The computed E_g in the spin-majority or spin-minority channel within GGA/GGA+U method for biaxial and hydrostatic strained systems are plotted in Fig. 5a,b, respectively. In the case of biaxial strain, a smooth decrease in E_g is evident for both (compressive and tensile) strains within GGA/GGA+U scheme, see Fig. 5a. A similar trend of reduction in E_g as a function of both (compressive and tensile) hydrostatic strain systems is also predicted (see Fig. 5b). However, a sharp decrease in E_g is established for a compressive strain of −1% within GGA+U in contrast to biaxially compressive strained system and then a very small decline in E_g is embedded upto −5%. It is important to note that E_g becomes zero for +2% hydrostatic tensile strained system (Fig. 5b), which means that the system exhibits FM metallic behavior as shown in TDOS of Fig. 4b′.

The decrease in the E_g can be explained by understanding the mutual hybridization between Cr/Re 3/5d and O 2p states. For this, we produced Cr 3d, Re 5d, and O 2p partial density of states (PDOS) for unstrained (0%) and biaxially compressive and tensile strained systems for instant in Figs. 4S and 5S of the SI within GGA scheme, respectively. From Fig. 4S, one can clearly see that partially occupied Cr 3d orbitals in the valence band strongly shift towards the higher energies as compared to unstrained (0%) system, when a biaxial compressive strain is adjusted from −1% to −5% (Fig. 4Sb–f of the SI), substantially reduced the E_g. This is attributed to a strong hybridization between Cr 3d and O 2p states because compressive strain enhanced the interaction between atoms and more orbitals overlap with each other. This results in the broadening of the bandwidth and decrease in E_g as discussed in these Refs.[41,55]. Moreover, a small shift of partially unoccupied Re 5d bands towards the lower energies in the conduction band can be seen, which also contribute to the reduction of E_g. Black dotted lines on the band edges of Cr and Re atoms in the valence and conduction bands are drawn for a guide to the eye, which clearly shows the shift of bands towards higher and lower energies, respectively. In the case of a tensile strain of +1% to +5%, Cr and Re bands position in the valence and conduction bands almost remains the same (Fig. 5Sb–f of the SI) as that of the unstrained system (Fig. 5Sa of the SI). However, a small shift of partially unoccupied Cr 3d orbitals in the conduction band from higher to lower energies occurs, which leads to a minute reduction of E_g (Fig. 5a). Hence, the decrease in E_g as a function of both type of strains in the remaining systems can also be explained as above discussed for a biaxially strained system within GGA approach.

To deeply understand the origin of the flipping of metallic electronic states from spin-minority to spin-majority channel in TDOS (Figs. 3b′, 4b′, c′) at the critical biaxial (+2%) and hydrostatic (+2% and +3%) tensile strains within GGA+U method, we produced the orbital resolved partial Cr 3d and Re 5d PDOS in Fig. 6. In
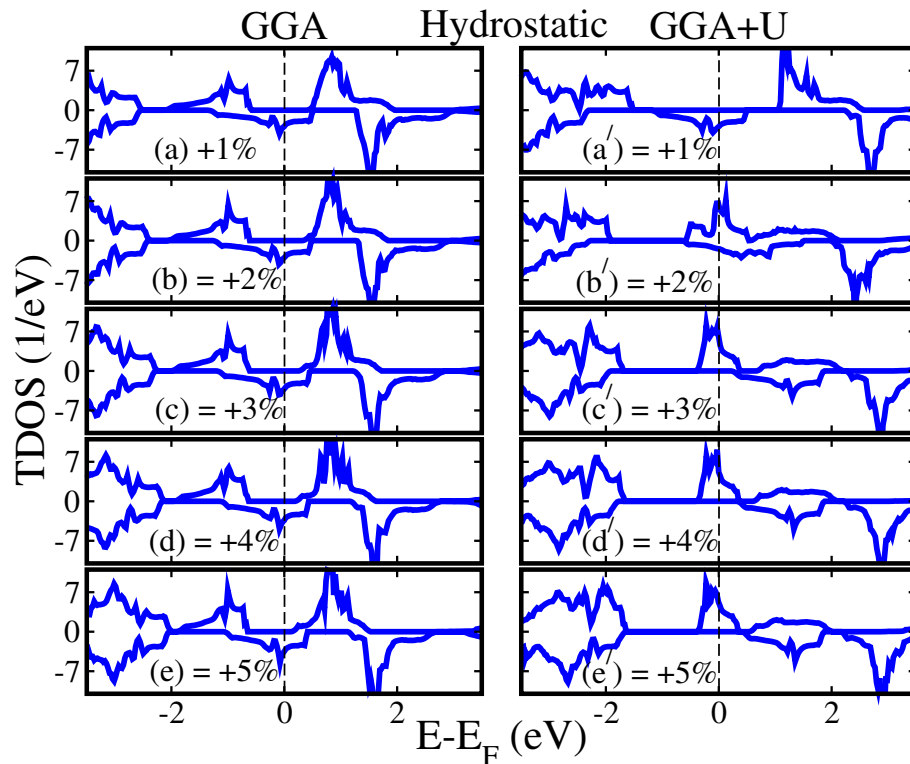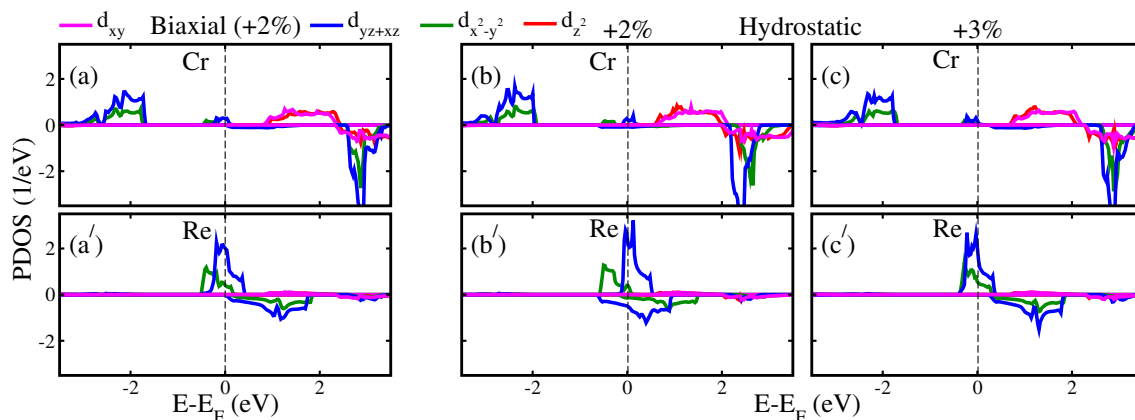
Figure 4. Calculated GGA/GGA+U spin-polarized total density of states (TDOS) of Sr_2CrReO_6 for (**a**, **a**′) +1%, (**b**, **b**′) +2%, (**c**, **c**′) +3%, (**d**, **d**′) +4%, and (**e**, **e**′) +5% hydrostatic tensile strains along [111]-direction.
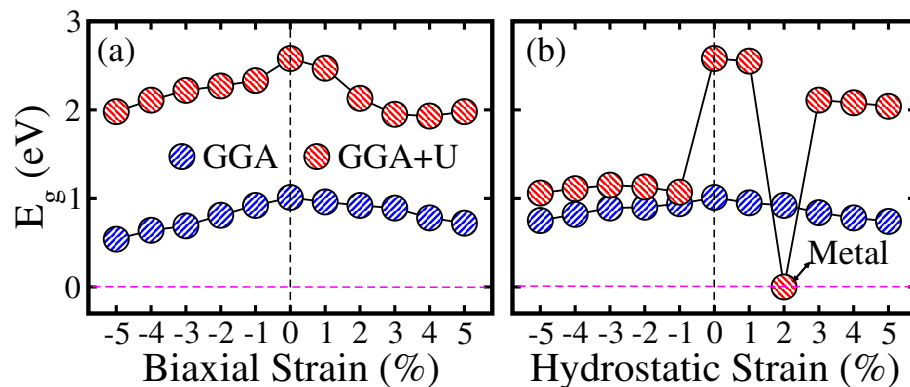

Figure 5. Calculated GGA and GGA+U energy band gap (E_g) in the spin-majority/minority channel of Sr_2CrReO_6 as a function of (**a**) biaxial [110] and (**b**) hydrostatic [111] strains.

the case of +2% biaxial strain system, a small contribution to the metallicity in the spin-majority channel comes from Cr d_{yz+xz} orbitals (Fig. 6a), while Re $d_{x^2-y^2}$ and d_{yz+xz} orbitals are mainly responsible for metallicity and also showing a strong hybridization near E_F (Fig. 6a′). It is important to note that Cr and Re states are not crossing E_F in the spin-minority channel, therefore this system is referred to HM. Moreover, Re $d_{x^2-y^2}$ and d_{yz+xz} metallic states flip from spin-minority to the spin-majority channel at a critical biaxial strain of +2% and also for higher strains as compared to unstrained (Fig. 2c′) and compressive/tensile strained system (Fig. 3). For the hydrostatic +2% tensile strain, a very small contribution to metallicity comes from Cr d_{yz+xz} orbitals in the spin-majority channel (Fig. 6b) as found in the case of +2% biaxial strain system (Fig. 6a). However, Re $d_{x^2-y^2}$ and d_{yz+xz} orbitals are mainly responsible for metallicity in the spin-majority channel along with a substantial contribution from spin-minority d_{yz+xz} orbitals (Fig. 6b′) in contrast to biaxial +2% tensile strain (Fig. 6a′). As both channels are metallic, therefore, this system is referred to FMM for +2% hydrostatic tensile strain. Similarly, almost a negligible contribution to metallicity comes from Cr spin-majority d_{yz+xz} states for +3% hydrostatic

Figure 6. Calculated GGA+U spin-polarized orbital resolved partial density of states (PDOS) of Cr/Re 3/5d in Sr$_2$CrReO$_6$ for (**a**, **a**′) biaxial +2% and hydrostatics (**b**, **b**′) +2% and (**c**, **c**′) +3% tensile strains.
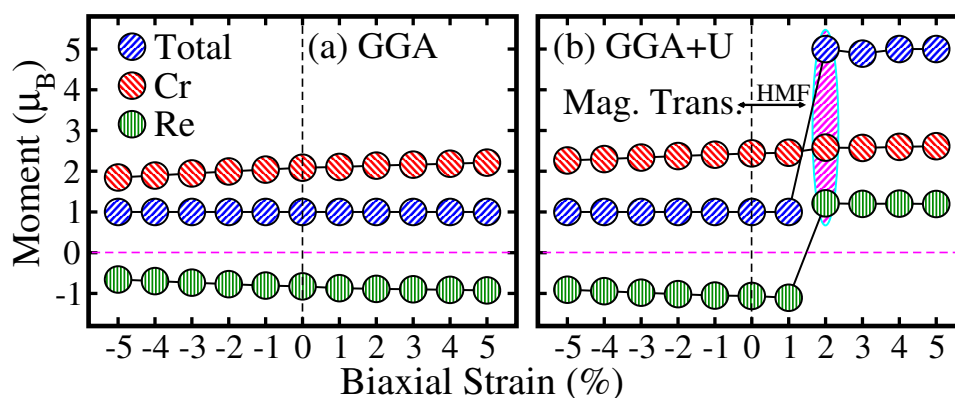

Figure 7. Calculated total and partial magnetic moments of Sr$_2$CrReO$_6$ within (**a**) GGA and (**b**) GGA+U schemes as a function of biaxial strains along the [110]-direction. The "−" and "+" signs indicate compressive and tensile strains, respectively. The shaded region (magenta color in **b**) represents the magnetic transition from half-metallic ferri-(HM FiM) to half-metallic ferromagnetic (HMF) state.

tensile strain (see Fig. 6c), while the spin-minority channel is insulator. On the other hand, Re $d_{x^2-y^2}$ and d_{yz+xz} orbitals in the spin-majority channel are primarily responsible for the conductivity as shown in Fig. 6c′. Interestingly, the spin-minority channel becomes insulator (no states are crossing the E_F) again for +3% tensile strain, which leads the system from HM to FM state.

Magnetic properties. Next, we examined the strain-induced changes of the magnetic moments in the SCRO system. The computed total and partial magnetic moments on the Cr/Re ions as a function of biaxial strains are plotted in Fig. 7. In the case of GGA, one can clearly see that Cr and Re magnetic moments are slight decreases from 2.09 to 1.85 μ_B and −0.83 to −0.66 μ_B when a biaxial strain is adjusted from 0% to −1.5% (Fig. 7a), respectively. On the other hand, moments slightly increases from 2.09 to 2.22 μ_B and −0.83 to −0.93 μ_B in the range of 0% to +1.5% (Fig. 7a), respectively. The "−" sing in the Re moments indicate that Cr and Re spins are anti-align (anti-parallel) and AFM coupling between them is favorable, which confirms the FiM magnetic ordering under-considered both compressive and tensile biaxial strains within GGA scheme as found in the case of the unstrained system. Similarly, a slight decrease (increase) in the magnitude of Cr and Re moment is evident for GGA+U method when a biaxial strain is adjusted from 0% to −5% (0% to +5%), see Fig. 7b. Here, it is very important to note that Re moment changes its sign from "−" to "+" at a critical +2% tensile strain, which means that Re spin is parallel to that of the Cr ion and this leads the magnetic phase transition from FiM to FM ordering. A similar trend is also established for +3% to +5% biaxial tensile strained systems. However, the total moment remains constant to an integral value of 1.0 μ_B for both GGA and GGA+U methods for strain ranges of −5% to +5% and −5% to +1%, respectively. In contrast, a total moment increases to an integral value of 5.0 μ_B within GGA+U scheme for the biaxial tensile strains of +2% to +5%. Because Re moment changes its sign from negative to positive and added to that of the Cr, which provides strengthen to the total moment. These integral values of the moments in all strained systems, confirms the HM nature as display in Fig. 3. Similarly, Lu et al.[41] also established a magnetic transition from FiM to FM in the SFMO system for a biaxial tensile strain of +7% using DFT calculations. As one can see that in the SFMO system, transition occurs at a very high biaxial tensile
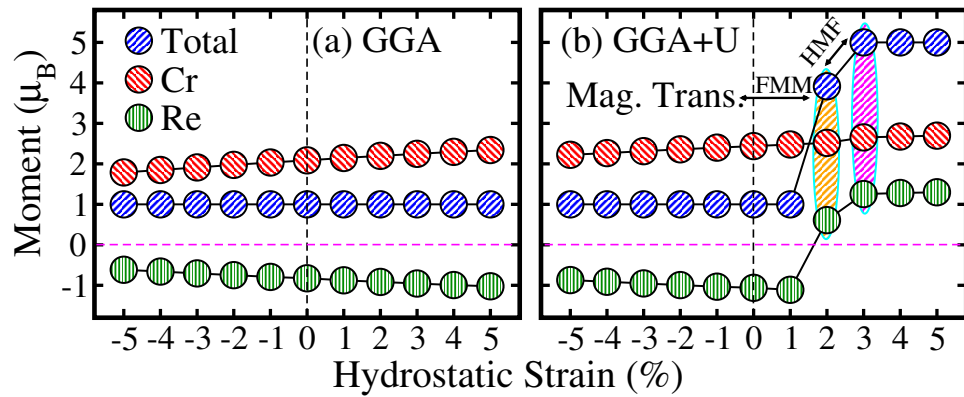
Figure 8. Calculated total and partial magnetic moments of Sr_2CrReO_6 within (**a**) GGA and (**b**) GGA+U schemes as a function of hydrostatic strains along the [111]-direction. First shaded region (orange color in **b**) represents the magnetic transition from half-metallic ferri- (HM FiM) to ferromagnetic metallic (FMM) state, while second (magenta color) indicates the FMM to HM ferromagnetic (HMF) transition.
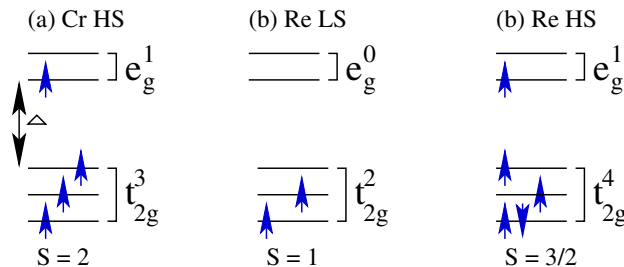
Figure 9. Schematic representation of (**a**) Cr high spin (HS), (**b**) Re low spin (LS), and Re intermediate spin (IS) states. Δ represents the enegy gap between t_{2g} and e_g states.

strain of +7%. However, our calculations reveal that a moderate biaxial strain of +2% is high enough to make a transition from HM FiM to HM FM in SCRO system, which is practically more feasible as found in the case of SFMO system.

Similary, the GGA calculated magnetic moments for both (compressive and tensile) hydrostatic strains exhibit a comparable trend and magnitudes (Fig. 8a) as found in the case of biaxial strain systems (Fig. 7a), as discussed above. The moments (total and partials) increases (decreases), when strain is adjusted from −5% to 0% (0% to +5%). For GGA+U scheme, the computed moments for hydrostatic strains of −5% to +1% (Fig. 8b) show the same behavior as established in the case of biaxially strained systems (Fig. 7b). Surprisingly, Re moment changes its sign from negative to positive at a critical tensile strain of +2%, which means that Re spin is parallel to that of Cr and results in a magnetic transition from FiM to FM. However, the total moment is 3.92 μ_B at this strain, which is not an integral value and also in contrast to biaxial +2% tensile strain system. Therefore, it is referred to FMM instead of HMF and confirms the calculated TDOS in Fig. 4b′. Interestingly, the system displays a second magnetic transition from FMM to HFM ordering at a tensile strain of +3% with a total integral moment of 5.0 μ_B. Because, Re moment sharply increases from 0.62 to 1.25 μ_B when strain is adjusted from +2% to +3%, which gives strengthen to the total moment (Fig. 8b). Hence, this integral moment leads the system to HMF ordering as displayed in TDOS of Fig. 4c′. Moreover, a similar pattern of moments is also established for hydrostatic tensile strains of +4% and +5% within GGA+U method, see Fig. 8b.

From the above calculated average moments of Cr ($\sim$2.0/2.4 μ_B) and Re ($\sim$0.9/1.1 μ_B) in both types of strains as well as in unstrained system within GGA/GGA+U, except for hydrostatic tensile strain of +2% in which Re moment is 0.61 μ_B, which means that Cr and Re atoms remain in the high and low spin (HS and LS) states, respectively. However, Re is almost in low spin (LS) state only for hydrostatic tensile strain of +2%. Usually, Cr HS, Re LS, and Re HS are described as $3d^4$ ($t_{2g}^3 e_g^1$) with S = 2, $5d^5$ ($t_{2g}^2 e_g^0$) with S = 1, and $5d^5$ ($t_{2g}^4 e_g^1$) with S = 3/2 spin states as shown in the schematic diagram of Fig. 9a–c, respectively.

Octahedra distortion. The moment variations with strain can be understood from the structural distortion of the $CrO_6(ReO_6)$ octahedron. Therefore, we plotted the locally distorted $CrO_6(ReO_6)$ octahedron for different strained systems in Fig. 10. The $CrO_6(ReO_6)$ octahedra of the biaxially compressive (−2%) and tensile (+2%) strained systems are displayed in Fig. 10a,b, while those of the hydrostatic compressive (−2%) and tensile (+2%) strained systems are depicted in Fig. 10d, e, respectively. For comparison, the distorted $CrO_6(ReO_6)$ octahedron in the unstrained (0%) system is shown in Fig. 10c. Our results show that Cr–O/Re–O bond length substan-
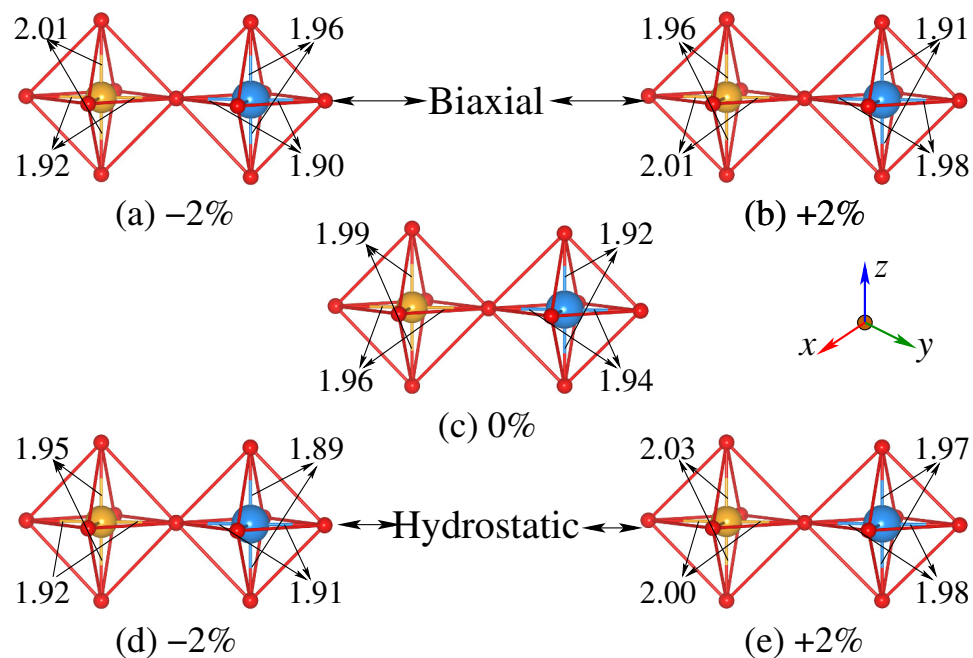
Figure 10. Locally distorted $CrO_6(ReO_6)$ octahedron in Sr_2CrReO_6 systems for (**a**) −2% and (**b**) +2% biaxial strains along the [110]-direction, (**c**) 0% (unstrained), and (**d**) −2% and (**e**) +2% hydrostatic strains along the [111]-direction. The x, y, and z-axes are along the crystallographic a, b, and c-directions, respectively.

tially increases from 1.92/1.90 Å to 1.96/1.94 Å in the ab-plane when driving from biaxially compressive (−2%) to tensile (+2%) strained systems (see Fig. 10a,b). Due to the expansion/reduction of Cr–O and Re–O bond lengths in the tensile/compressive (+2%/ − 2%) strained system (Fig. 10a, b) as compared to unstrained (0%) one (Fig. 10c), results in decreased/increased of the electrons hoping. Therefore, Cr and Re moments becomes larger and smaller due to highly confined and unconfined of spatial charge distribution around these atoms, respectively. Moreover, small elongation and suppression of Cr–O/Re–O bond length in the c-axis for biaxial compressive (Fig. 10a) and tensile (Fig. 10b) is evident than that of the unstrained system (Fig. 10c), respectively.

In the case of compressive (−2%) hydrostatic strain, Cr–O/Re–O bond length shorten along the ab-plane (Fig. 10d) as compared to the unstrained system (Fig. 10c), which is almost similar to the biaxially compressive (−2%) strained system (Fig. 10a). Along with this, Cr–O/Re–O bond length also decreases along the c-axis for −2% strain (Fig. 10d) as compared to unstrained one (Fig. 10c), which is in contrast to biaxially compressive strained system (Fig. 10a). The decrease in the bond lengths along the ab-plane results in smaller Cr/Re moments due to degradation of the spatial charge distribution as discussed above. However, Cr/Re moments increases because of the lengthening of the Cr–O/Re–O bond length along the [110]-direction for hydrostatic tensile (+2%) strain (Fig. 10e) than that of the unstrained system (Fig. 10c), as also determined in the case of biaxially tensile (+2%) system (Fig. 10b). Furthermore, the Cr–O/Re–O bond length also increases along the c-axis for hydrostatic tensile (+2%) strain, which is in contrast to biaxial tensile (+2%) strain system. Hence, one can conclude that elongation and contraction of bond lengths can substantially be enhanced and reduced the magnetic moments due to confinement and degradation of spatial charge distribution, respectively.

Conclusion

In summary, the electronic and magnetic properties of unstrained and strained (biaxial and hydrostatic) Sr_2CrReO_6 systems were investigated using spin-polarized density functional theory. Our calculations revealed that antiferromagnetic (AFM) coupling between Cr and Re, while ferromagnetic (FM) couplings are energetically favorable between the similar (Cr/Cr and Re/Re) ions, results in ferrimagnetic (FiM) ground state for the unstrained SCRO system. Furthermore, it is demonstrated that only Re spin-minority d_{yz+xz} and $d_{x^2-y^2}$ states are mainly responsible for metallicity, which leads the system to half-metal (HM) FiM. The HM nature shows the robustness as a function of both kinds of strains. Interestingly, a magnetic transition from HM FiM to HM FM is established for +2% biaxial tensile strain within GGA+U method due to flipping of Re spin alignment to that of Cr ion. On the other hand, two magnetic transitions: (1) a HM FiM to FM metal (FMM) and (2) FMM to HM FM are found in the case of hydrostatic tensile strains of +2% and +3% for GGA+U method, respectively. Strong confinement of orbitals due to tensile strains, leads to the decrease of electron hoping and also reduced the AFM coupling strength between Cr and Re atoms, which results in FiM-to-FM transition. Thus, we propose that magnetic properties of the perovskite oxide systems can be optimized by applying a moderate tensile strain along the [110] and [111]-directions.

Computational methods

Full-potential linearized augmented plane wave method of spin-polarized DFT as implemented in the WIEN2K code[56] is used. The generalized gradient approximation (GGA), which is parameterized by Perdew-Burke-Ernzerhof (PBE)[57] plus on-site Coulomb interaction (GGA+U) approach was employed with $U = 3.5$ and 2.4 eV for Cr 3d and Re 5d states, respectively[58]. For the wave function expansion inside the atomic spheres, a maximum value of $l_{max} = 12$ is chosen and the plane-wave cutoff is set to $R_{mt} \times K_{max} = 7$ with $G_{max} = 24$. A $10 \times 10 \times 9$ k-space grid with 102 points within the irreducible wedge of the Brillouin zone is found to be well converged. Along with this, full relaxation of the atomic positions by minimizing the atomic forces up to 2 mRy/a.u is taken into account in each case. Self-consistency is assumed for a total energy convergence of less than 10^{-5} Ry.

References

1. Boeck, J. D. *et al.* Technology and materials issues in semiconductor-based magnetoelectronics. *Semicond. Sci. Technol.* **170**, 342. https://doi.org/10.1088/0268-1242/17/4/307 (2002).
2. Katsnelson, M. I., Irkhin, V. Y., Chioncel, L., Lichtenstein, A. & de Groot, R. A. Half-metallic ferromagnets: from band structure to many-body effects. *Rev. Mod. Phys.* **80**, 315. https://doi.org/10.1103/RevModPhys.80.315 (2008).
3. Zutic, I., Fabian, J. & Sarma, S. D. Spintronics: fundamentals and applications. *Rev. Mod. Phys.* **76**, 323. https://doi.org/10.1103/RevModPhys.76.323 (2004).
4. Kobayashi, K. I., Kimura, T., Sawada, H., Terakura, K. & Tokura, Y. Room-temperature magnetoresistance in an oxide material with an ordered double-perovskite structure. *Nature* **395**, 677. https://doi.org/10.1038/27167 (1998).
5. Salamon, M. B. & Jaime, M. The physics of manganites: structure and transport. *Rev. Mod. Phys.* **73**, 583. https://doi.org/10.1103/RevModPhys.73.583 (2001).
6. Brataas, A., Kent, A. D. & Ohno, H. Current-induced torques in magnetic materials. *Nat. Mater.* **11**, 372. https://doi.org/10.1038/nmat3311 (2012).
7. Kent, A. D. & Worledge, D. C. A new spin on magnetic memories. *Nat. Nanotechnol.* **10**, 187. https://doi.org/10.1038/nnano.2015.24 (2015).
8. Dieny, B. & Chshiev, M. Perpendicular magnetic anisotropy at transition metal/oxide interfaces and applications. *Rev. Mod. Phys.* **89**, 025008. https://doi.org/10.1103/RevModPhys.89.025008 (2017).
9. Kumari, K. *et al.* Structural and resistive switching behaviour in lanthanum strontium manganite-reduced graphene oxide nanocomposite system. *J. Alloys Compd.* **815**, 152213. https://doi.org/10.1016/j.jallcom.2019.152213 (2020).
10. Dayen, J.-F., Ray, S. J., Karis, O., Vera-Marun, I. J. & Kamalakar, M. V. Two-dimensional van der waals spinterfaces and magnetic-interfaces. *Appl. Phys. Rev.* **7**, 011303. https://doi.org/10.1063/1.5112171 (2020).
11. Serrate, D., Teresa, J. M. D. & Ibarra, M. R. Double perovskites with ferromagnetism above room temperature. *J. Phys. Condens. Matter* **19**, 023201. https://doi.org/10.1088/0953-8984/19/2/023201 (2007).
12. Kato, H. *et al.* Structural and electronic properties of the ordered double perovskites $A_2 M ReO_6$ (A=Sr, Ca; M=Mg, Sc, Cr, Mn, Fe Co, Ni, Zn). *Phys. Rev. B* **69**, 184412. https://doi.org/10.1103/PhysRevB.69.184412 (2004).
13. Rubi, D. *et al.* Spectroscopic investigation on the influence of AS defects on the electronic structure of $Sr_2 FeMoO_6$. *J. Phys. Chem. Solids* **67**, 575. https://doi.org/10.1016/j.jpcs.2005.10.123 (2006).
14. Paturi, P., Metsnoja, M. & Huhtinen, H. Optimization of deposition temperature and atmosphere for pulsed laser deposited $Sr_2 FeMoO_6$ thin films. *Thin Solid Films* **519**, 8047. https://doi.org/10.1016/j.tsf.2011.06.059 (2011).
15. Saloaro, M. *et al.* The predominance of substrate induced defects in magnetic properties of $Sr_2 FeMoO_6$ thin films. *J. Phys. Condens. Matter* **27**, 386001. https://doi.org/10.1088/0953-8984/27/38/386001 (2015).
16. Hoffmann, M. *et al.* Variation of magnetic properties of $Sr_2 FeMoO_6$ due to oxygen vacancies. *J. Phys. Condens. Matter* **30**, 305801. https://doi.org/10.1088/1361-648X/aacb8d (2018).
17. Patterson, F. K., Moeller, C. W. & Ward, R. Magnetic oxides of molybdenum(V) and tungsten(V) with the ordered perovskite structure. *Inorg. Chem.* **2**, 196. https://doi.org/10.1021/ic50005a050 (1963).
18. Galasso, F. S. *Structure, Properties and Preparation of Perovskite-Type Compounds* 1st edn. (Pergamon, London, 1969).
19. Wolf, S. A. *et al.* Spintronics: a spin-based electronics vision for the future. *Science* **294**, 1488. https://doi.org/10.1126/science.1065389 (2001).
20. Kato, H., Okuda, T., Okimoto, Y. & Tomioka, Y. Metallic ordered double-perovskite $Sr_2 CrReO_6$ with maximal curie temperature of 635 K. *Appl. Phys. Lett.* **81**, 328. https://doi.org/10.1063/1.1493646 (2002).
21. Asano, H., Kozuka, N., Tsuzuki, A. & Matsui, M. Growth and properties of high-curie-temperature $Sr_2 CrReO_6$ thin films. *Appl. Phys. Lett.* **85**, 263. https://doi.org/10.1063/1.1769085 (2004).
22. Majewski, P., Geprgs, S., Sanganas, O., Opel, M. & Gross, R. X-ray magnetic circular dichroism study of Re 5d magnetism in $Sr_2 CrReO_6$. *Appl. Phys. Lett.* **87**, 202503. https://doi.org/10.1063/1.2131178 (2005).
23. Lee, A. T. & Marianetti, C. A. Structural and metal-insulator transitions in rhenium-based double perovskites via orbital ordering. *Phys. Rev. B* **97**, 045102. https://doi.org/10.1103/PhysRevB.97.045102 (2018).
24. Philipp, J. B. *et al.* Spin-dependent transport in the double-perovskite $Sr_2 CrWO_6$. *Appl. Phys. Lett.* **79**, 3654. https://doi.org/10.1063/1.1421227 (2002).
25. Philipp, J. B. *et al.* Structural and doping effects in the half-metallic double perovskite $A_2 CrWO_2$ (A = Sr, Ba, and Ca). *Phys. Rev. B* **68**, 144431. https://doi.org/10.1103/PhysRevB.68.144431 (2003).
26. Krockenberger, Y. *et al.* A neutron scattering study of the crystal and magnetic structure of $Sr_2 CrOsO_2$. *J. Magn. Magn. Mater.* **310**, 1854. https://doi.org/10.1016/j.jmmm.2006.10.648 (2007).
27. Krockenberger, Y. *et al.* $Sr_2 CrOsO_2$: end point of a spin-polarized metal-insulator transition by 5d band filling. *Phys. Rev. B* **75**, 020404. https://doi.org/10.1103/PhysRevB.75.020404 (2007).
28. Lee, K. W. & Pickett, W. E. Half semimetallic antiferromagnetism in the $Sr_2 CrTO_6$ system ($T =$ Os and Ru). *Phys. Rev. B* **77**, 115101. https://doi.org/10.1103/PhysRevB.77.115101 (2008).
29. Vaitheeswaran, G., Kanchana, V. & Delin, A. Half semimetallic antiferromagnetism in the $Sr_2 Cr TO_6$ system ($T =$ Os and Ru). *Appl. Phys. Lett.* **86**, 032513. https://doi.org/10.1063/1.1855418 (2005).
30. Borges, R. P. *et al.* Thin films of the double perovskite $Sr_2 FeMoO_6$ deposited by pulsed laser deposition. *Thin Solid Films* **429**, 5. https://doi.org/10.1016/S0040-6090(03)00009-9 (2003).
31. Fix, T. *et al.* Effects of strain relaxation on the electronic properties of epitaxial $Sr_2 FeMoO_6$ grown by pulsed laser deposition on $SrTiO_3$ (001). *J. Appl. Phys.* **98**, 023712. https://doi.org/10.1063/1.1925761 (2005).
32. Jalili, H., Heinig, N. F. & Leung, K. T. X-ray photoemission study of $Sr_2 FeMoO_6$ and $SrMoO_4$ films epitaxially grown on MgO(001): near-surface chemical-state composition analysis. *Phys. Rev. B* **79**, 174427. https://doi.org/10.1103/PhysRevB.79.174427 (2009).

33. Chu, M., Sun, Y., Aghoram, U. & Thompson, S. E. Strain: a solution for higher carrier mobility in nanoscale mosfets. *Annu. Rev. Mater. Res.* **39**, 203. https://doi.org/10.1146/annurev-matsci-082908-145312 (2009).

34. Jalan, B. *et al.* Enhancing the electron mobility of SrTiO$_3$ with strain. *Appl. Phys. Lett.* **98**, 132102. https://doi.org/10.1063/1.3571447 (2011).

35. Bark, C. W. *et al.* Tailoring a two-dimensional electron gas at the LaAlO$_3$/SrTiO$_3$ (001) interface by epitaxial strain. *Proc. Natl. Acad. Sci. USA* **108**, 4720. https://doi.org/10.1073/pnas.1014849108 (2011).

36. Kalisky, B. *et al.* Locally enhanced conductivity due to the tetragonal domain structure in LaAlO$_3$/SrTiO$_3$ heterointerfaces. *Nat. Mater.* **12**, 1091 (2013).

37. Du, C. H. *et al.* Control of magnetocrystalline anisotropy by epitaxial strain in double perovskite Sr$_2$FeMoO$_6$ films. *Phys. Rev. Lett.* **110**, 147204. https://doi.org/10.1103/PhysRevLett.110.147204 (2013).

38. Yang, K., Setyawan, W., Wang, S., Nardelli, M. B. & Curtarolo, S. A search model for topological insulators with high-throughput robustness descriptors. *Nat. Mater.* **11**, 614. https://doi.org/10.1038/nmat3332 (2012).

39. Qian, Y. *et al.* Effect of high-pressure on the electronic and magnetic properties in double perovskite oxide Sr$_2$FeMoO$_6$. *J. Appl. Phys.* **112**, 103712. https://doi.org/10.1063/1.4768195 (2012).

40. Qian, Y. *et al.* Biaxial strain effect on the electronic and magnetic phase transitions in double perovskite La$_2$FeMnO$_6$: a first-principles study. *J. Appl. Phys.* **114**, 063713. https://doi.org/10.1063/1.4818321 (2013).

41. Lu, R. *et al.* The effect of biaxial mechanical strain on the physical properties of double perovskite Sr$_2$FeMoO$_6$: a theoretical study. *Solid State Commun.* **191**, 70. https://doi.org/10.1016/j.ssc.2014.03.017 (2014).

42. Nazir, S., Behtash, M. & Yang, K. Enhancing interfacial conductivity and spatial charge confinement of LaAlO$_3$/SrTiO$_3$ hetero-structures via strain engineering. *Appl. Phys. Lett.* **105**, 141602. https://doi.org/10.1063/1.4897626 (2014).

43. Nazir, S. & Yang, K. First-principles characterization of the critical thickness for forming metallic states in strained LaAlO$_3$/SrTiO$_3$ (001) heterostructure. *ACS Appl. Mater. Interfaces* **6**, 22351. https://doi.org/10.1021/am506336w (2014).

44. Nazir, S., Behtash, M. & Yang, K. The role of uniaxial strain in tailoring the interfacial properties of LaAlO$_3$/SrTiO$_3$ heterostructure. *RSC Adv.* **5**, 15682. https://doi.org/10.1039/C4RA15866K (2015).

45. Zulfiqar, M., Zhao, Y., Li, G., Nazir, S. & Ni, J. Tunable conductivity and half metallic ferromagnetism in monolayer platinum diselenide: a first-principles study. *J. Phys. Chem. C* **120**, 25030. https://doi.org/10.1021/acs.jpcc.6b06999 (2016).

46. Hauser, A. J. *et al.* Fully ordered Sr$_2$CrReO$_6$ epitaxial films: a high-temperature ferrimagnetic semiconductor. *Phys. Rev. B* **85**, 161201. https://doi.org/10.1103/PhysRevB.85.161201 (2012).

47. Teresa, J. M. D. *et al.* Investigation of the high curie temperature in Sr$_2$CrReO$_6$. *Phys. Rev. B* **71**, 092408. https://doi.org/10.1103/PhysRevB.71.092408 (2005).

48. Winkler, A. *et al.* Magnetism in Re-based ferrimagnetic double perovskites. *New J. Phys.* **11**, 073047. https://doi.org/10.1088/1367-2630/11/7/073047 (2009).

49. Olsen, J. S., Gerward, L., Vaitheeswaran, G., Kanchana, V. & Alff, L. High-pressure structural behavior of the double perovskite Sr$_2$CrReO$_6$: an experimental and theoretical study. *High Press Res.* **29**, 83–86. https://doi.org/10.1080/08957950802429045 (2009).

50. Gutlich, P. & Goodwin, H. *Spin Crossover in Transition Metal Compounds* (Springer, Berlin, 2004).

51. Nair, A. K., Kumari, P., Kamalakar, M., Venkata, M. & Ray, S. J. Dramatic magnetic phase designing in phosphorene. *Phys. Chem. Chem. Phys.* **21**, 23713–23719. https://doi.org/10.1039/C9CP04871E (2019).

52. Tang, C. Q., Zhang, Y. & Dai, J. Electronic and magnetic structure studies of double perovskite Sr$_2$CrReO$_6$ by first-principles calculations. *Solid State Commun.* **133**, 219–222. https://doi.org/10.1016/j.ssc.2004.11.006 (2005).

53. Vaitheeswaran, G., Kanchana, V. & Delin, A. Electronic structure of the ferromagnetic double-perovskites Sr$_2$CrReO$_6$, Sr$_2$CrWO$_6$, and Ba$_2$FeReO$_6$. *Solid State Commun.* **50–53**, 219–222. https://doi.org/10.1088/1742-6596/29/1/008 (2006).

54. Mandal, T. K., Felser, C., Greenblatt, M. & Käbler, J. Magnetic and electronic properties of double perovskites and estimation of their curie temperatures by ab initio calculations. *Phys. Rev. B* **78**, 134431. https://doi.org/10.1103/PhysRevB.78.134431 (2008).

55. Hung, Y. C., Jiang, J. C., Chao, C. Y., Su, W. F. & Lin, S. T. Theoretical study on the correlation between band gap, bandwidth, and oscillator strength in fluorene-based donor-acceptor conjugated copolymers. *J. Phys. Chem. B* **113**, 8268. https://doi.org/10.1021/jp9018603 (2009).

56. Blaha, P., Schwarz, K., Sorantin, P. & Trickey, S. B. Full-potential, linearized augmented plane wave programs for crystalline systems. *Comput. Phys. Commun.* **59**, 399. https://doi.org/10.1016/0010-4655(90)90187-6 (1990).

57. Perdew, J. P., Burke, K. & Ernzerhof, M. Generalized gradient approximation made simple. *Phys. Rev. Lett.* **77**, 3865. https://doi.org/10.1103/PhysRevLett.77.3865 (1996).

58. Calderon, C. E. *et al.* The aflow standard for high-throughput materials science calculations. *Comput. Mater. Sci.* **108**, 233. https://doi.org/10.1016/j.commatsci.2015.07.019 (2015).

Author contributions

Q.A. and S.Nas. conducted the calculations and S.Naz. wrote the manuscript.

Competing interests

The authors declare no competing interests.

Additional information

Supplementary information is available for this paper at https://doi.org/10.1038/s41598-020-70768-7.

Correspondence and requests for materials should be addressed to S.N.

Reprints and permissions information is available at www.nature.com/reprints.

Publisher's note Springer Nature remains neutral with regard to jurisdictional claims in published maps and institutional affiliations.